RESEARCH ARTICLE

NANO · MICRO small
www.small-journal.com

Long-Term Diabetic Retinopathy Treatment Using Silicon Nanoneedles

Van Phuc Nguyen, Jinheon Jeong, Mi Zheng, Junsang Lee, Josh Zhe, Zhuying Wei, Chi Hwan Lee, and Yannis M. Paulus**

Sustained-release ocular drug delivery systems with minimal invasiveness are critical for managing eye diseases that cause blindness. An innovative platform is presented for painless and long-term sustained ocular drug delivery utilizing controllably biodegradable silicon nanoneedles (Si NNs) conjugated with bevacizumab (Bev) integrated into a tear-soluble subconjunctival patch. The biocompatible patch facilitates easy application in the subconjunctival area of the eye and rapid dissolution in less than one minute upon contact with the tear film in the sclera, eliminating the need for removal procedures. The Si NNs, fabricated with precise control over their degradation kinetics, enable sustained and controlled release of Bev into the ocular tissues. This platform offers enhanced patient comfort, reduced risk of complications, and prolonged therapeutic efficacy. In vivo studies using a rabbit model of retinal neovascularization (RNV), a clinically relevant proliferative diabetic retinopathy (PDR), demonstrate the platform's ability to reduce RNV by 85% over a year, with no observable side effects. These results highlight the potential of this drug delivery method to penetrate the sclera and releaseBev gradually, providing a promising alternative for long-term, controllable ocular therapy. This technology represents a significant advancement in painless, convenient, and effective treatment for eye diseases requiring sustained drug delivery.

1. Introduction

Diabetes mellitus is a rapidly increasing health burden that is projected to affect 592 million people by 2035.[1] Diabetes can cause numerous cardiac complications as well as nerve damage and also debilitating effects on vision. Diabetic retinopathy (DR) was estimated to have affected 103 million individuals worldwide in 2020 and is projected to increase to 160 million by 2045.[2] Uncontrolled chronic hyperglycemia, the primary pathogenic agent in DR, activates glucose metabolism pathways, whose end products cause increased vascular permeability as well as the blockage of small blood vessels. Hyperglycemia and hypoxia can upregulate the expression of vascular endothelial growth factor (VEGF), which plays a key role in both blood-retinal barrier (BRB) disruption and retinal neovascularization. The uncontrolled neovascularization caused by increased level of VEGF with a leaky retinal microvasculature can ultimately result in blindness.[3–5] DR can be

V. P. Nguyen, M. Zheng, Y. M. Paulus
Department of Ophthalmology
Wilmer Eye Institute
Johns Hopkins University
Baltimore, MD 21287, USA
E-mail: ypaulus1@jh.edu

V. P. Nguyen, M. Zheng, J. Zhe, Y. M. Paulus
Department of Ophthalmology and Visual Sciences
University of Michigan
Ann Arbor, MI 48105, USA

J. Jeong, J. Lee, C. H. Lee
Weldon School of Biomedical Engineering
Purdue University
West Lafayette, IN 47907, USA
E-mail: lee2270@purdue.edu

M. Zheng
Ophthalmology Department
Fujian Provincial Hospital
Fuzhou, Fujian 350001, China

Z. Wei
Center for Advanced Models for Translational Sciences and Therapeutics
University of Michigan
Ann Arbor, MI 48109, USA

C. H. Lee
School of Mechanical Engineering
Purdue University
West Lafayette, IN 47907, USA

C. H. Lee
School of Materials Engineering
Purdue University
West Lafayette, IN 47907, USA

C. H. Lee
Elmore School of Electrical and Computer Engineering
Purdue University
West Lafayette, IN 47907, USA

C. H. Lee
Birck Nanotechnology Center
Purdue University
West Lafayette, IN 47907, USA

The ORCID identification number(s) for the author(s) of this article can be found under https://doi.org/10.1002/smll.202410166

DOI: 10.1002/smll.202410166

grouped into two forms: the earlier nonproliferative diabetic retinopathy (NPDR) and the more advanced proliferative diabetic retinopathy (PDR). NPDR is mainly characterized by microaneurysms, exudates, and intraretinal bleeding, while PDR is characterized by retinal neovascularization.[6–8]

Current popular methods of DR treatment include pharmacotherapy, laser therapy, and combination therapy.[9,10] The majority of DR drugs fall under anti-vascular endothelial growth factor agents (anti-VEGF) such as bevacizumab, ranibizumab, and aflibercept. Intravitreal ranibizumab injection has been shown to be an effective treatment method through a 2010 phase 3, randomized clinical trial for diabetic macular edema (DME).[11] However, the study required monthly intravitreal injections, which are invasive, require frequent administration, and carry significant risks including the risk of eye infection (endophthalmitis). Unfortunately, this is unavoidable as anti-VEGF biologics have a short half-life, and the majority of drug payload fails to reach their target destination due to anatomical barriers in the eye.[12–15] Laser therapy is theorized to stop microvasculature leakage as well as decrease the production of VEGF factors.[16] Pairing anti-VEGF treatment with photocoagulation laser therapy has shown more robust and lasting protection from neovascularization; however, it can also result in permanent blind spots in the peripheral visual field and worsen night vision in patients.[17] Newer laser therapy methods known as subthreshold pulses have been shown to be able to deliver therapy without any noticeable lesions and loss in visual acuity, but have not yet proven their efficacy in large, prospective, randomized clinical trials of patients with PDR.[18]

While anti-VEGF treatment of DME and RNV is still the standard, the current intravitreal injection delivery of the drug is invasive and not dose-efficient. Anatomical structures such as the inner limiting membrane (ILM) prevent the majority of the drug payload from reaching its retinal targets. The ILM is also found to thicken with age, potentially decreasing the efficacy of intravitreal injections even further in elderly patients.[19] Although many methods of disrupting the ILM to increase retinal drug delivery have been studied, such as ILM peeling and photoablation of the ILM, they require another procedure in addition to the injections which is invasive and burdensome for clinical translation.[20,21] This study examines the efficacy of subconjunctival delivery of anti-VEGF through a novel silicon nanoneedle (Si NNs) subconjunctival patch to treat PDR and retinal neovascularization (RNV).

Si NNs allow for a non-invasive and painless method of applying therapeutic agents to deeper eye structures without having to penetrate the ILM. In our research, the Si NNs are applied to the sclera using a water-soluble subconjunctival patch, which dissolves within a minute and leaves the embedded Si NNs for an initial burst and subsequent long-term release of drugs. While the overall length of the Si NNs is in the micrometer range, the tip diameters and critical structural elements, which are essential for effective ocular penetration, are at the nanometer scale. These nanoscale features play a pivotal role in enabling precise and minimally invasive insertion into ocular tissues, distinguishing Si NNs from traditional microneedles. Long-term sustained release of pharmacological agents can be achieved by using a passivation layer made from compounds such as aluminum oxide, which slows the degradation of the Si NNs. While there are multiple composites used for nanoneedles other than silicon, such as poly(lactic-co-glycolic) acid (PLGA) and methacrylate hyaluronic acid, silicon has the slowest degradation rate in physiologic conditions. The Si NNs degrade at a rate of < 20nn/day, while PLGA and methacrylate hyaluronic acid degrade at a rate of 24 to 120 μm/day.[22–24]

2. Results

2.1. Sclera Embedded Si NNs Patch Fabrication

Figure 1a delineates the integration process of our biodegradable ocular drug delivery patch, which incorporates silicon nanoneedles (Si NNs) created from a bulk silicon wafer. The Si NNs were fabricated using standard microfabrication techniques, which include photolithographic patterning and a combination of dry and wet etching to achieve undercuts at the base and nanopores on the surfaces.[22] Detailed information on the fabrication steps can be found in the Experimental Section. The integration with our patch was achieved by transfer printing the Si NNs from the bulk Si wafer onto a biodegradable film, such as polyvinyl alcohol (PVA). The process commenced with the deposition of a polymethyl methacrylate (PMMA) film on the Si NNs via spin-coating, which acted as a sacrificial layer. Subsequently, a constant-rate mechanical peeling of the PMMA film was conducted using an automated peeling apparatus. During peeling, mechanical stresses concentrated at the undercuts induced separation of the Si NNs from the Si wafer.[25] PVA solution (2% wt) was then drop-cast onto the exposed Si NNs, followed by thermal polymerization at 60 °C for one hour in a vacuum chamber, repeated thrice to achieve a film thickness of ≈40 μm. The final stage involved removing the PMMA layer by immersion in 70 °C acetone for 4 h, then the film was rinsed with anhydrous ethanol and sterilized under UV light.

To enable effective drug attachment to the surface of Si NNs, covalent bonding is employed to ensure high binding affinity and prevent drug leakage during release. This process involves treating the Si NN surface with 3-triethoxysilylpropyl succinic anhydride (TESPSA), which facilitates the creation of amide bonds with antibody-based ocular drugs such as Bev. Then, the Si NNs patch was immersed in a diluted Bev solution for covalent bonding. The production process was carefully designed to preserve the bioactivity of Bev by avoiding harsh conditions, such as extreme pH or high temperatures, that could denature the protein. These measures were intended to ensure that the therapeutic efficacy of Bev remained uncompromised. Additionally, the conjugation reaction was conducted under controlled conditions to minimize potential structural alterations of the drug, further

Y. M. Paulus
Department of Biomedical Engineering
Johns Hopkins University
Baltimore, MD 21287, USA
Y. M. Paulus
Department of Biomedical Engineering
University of Michigan
Ann Arbor, MI 48105, USA

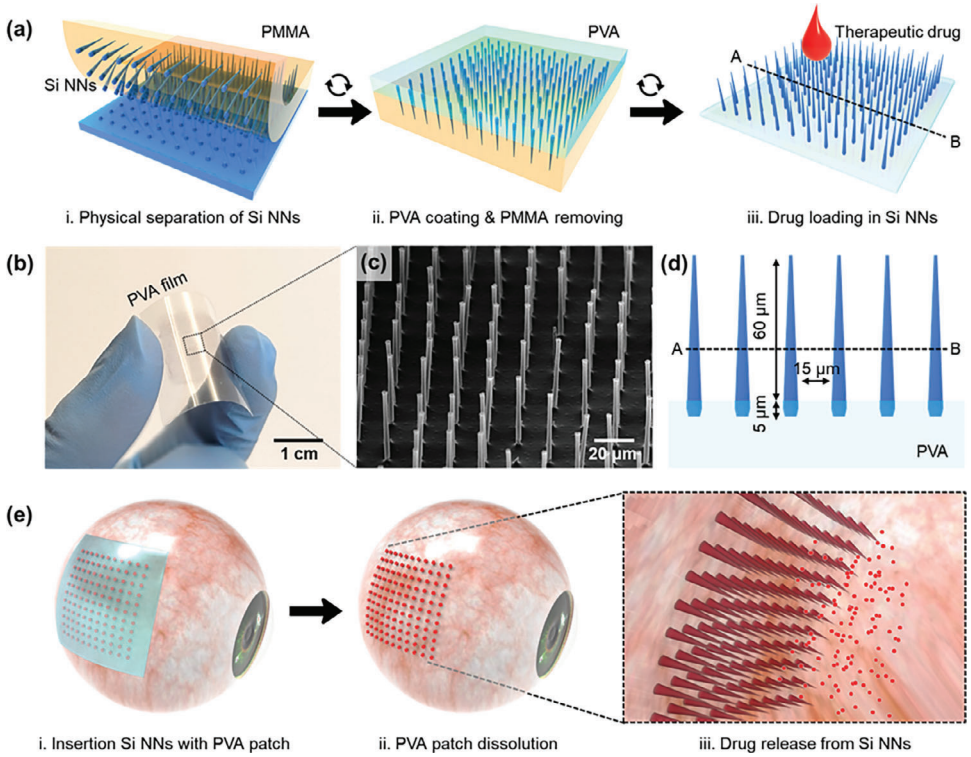

Figure 1. Structure and working principle of the biodegradable patch integrated with Si NNs. a) Schematic illustrations of the basic procedure for transferring Si NNs from a silicon wafer to a PVA film. b) Optical photograph of the biodegradable ocular drug delivery patch. c) SEM image of the Si NNs transferred onto the PVA film. d) Front-view depiction of the device structure for the biodegradable ocular drug delivery patch. e) Schematic diagrams illustrating the drug delivery process.

supporting its stability and functionality during and after patch fabrication.

Figure 1b showcases the completed patch with embedded Si NNs. The transfer process achieved a high yield (≥ 99%) of Si NNs across the patch, as verified by the SEM image in Figure 1c. Figure 1d specifies the dimensions of the transferred Si NNs on the PVA film, with the needles embedded 5 μm beneath the PVA surface and protruding for 60 μm. This design enables an effective puncture depth of ≈80 μm into the targeted tissue, ensuring efficient therapeutic delivery while minimizing damage to deeper ocular structures, such as the corneal stroma.[22] The functional principle of our patch is illustrated in Figure 1e. Application of the patch to the ocular surface allows for the smooth insertion of Si NNs into the sclera (Figure 1e, left). The patch then rapidly dissolves in tear fluid within a minute (Figure 1e, middle), while the Si NNs slowly degrade in the sclera over the course of months through hydrolysis into silicic acid and hydrogen,[26–28] enabling a sustained, long-term release of drugs (Figure 1e, right).

2.2. In Vivo Monitoring of Si NNs Treatment Using Color Fundus Photography and Fluorescein Angiography Imaging

After fabricating the sclera-embedded Si NNs patch conjugated with bevacizumab (Si NNs-Bev), we initiated treatment on pigmented rabbits with DR models. The DR models were established through intravitreal injection (IVT) of DL-alpha-aminoadipic acid (DL-AAA), following the protocol described in our group's previous studies. By day 7 post-IVT injection, all rabbits exhibited new retinal neovascularization (RNV). At this stage, the animal models were classified into four groups: one group received treatment with Si NNs-Bev patches, another was treated with Si NNs without Bev, a third group received intravitreal Bev only, and the fourth group served as a control without any treatment. Each group consisted of three rabbits with DR animal models. The treatment progression of Si NNs-Bev on RNV is monitored by a multimodal imaging system including color fundus photography, fluorescein angiography (FA), optical coherence tomography (OCT), and photoacoustic microscopy (PAM). **Figures** 2a–g and S1a–g (Supporting Information) displays the color fundus of RNV obtained at various intervals from day 0 to 12 months post-treatment, illustrating distinct differences between the groups treated with Si NNs-Bev (Figure 2g) and control groups: untreated (Figure 2a), Bev (Figure 2c), and Si NNs (Figure 2e). In the treated group with Si NNs-Bev, retinal vessels (RVs) were evident alongside reduced RNV and intact optic nerves. Conversely, the untreated group, Bev and Si NNs display heightened vessel tortuosity and density one month after treatment. However, from the second month onward, there was a gradual decrease in vessel tortuosity, which stabilized at an elevated level for up to 12 months. Figure 2b–h and Figure S1b–h (Supporting Information) depict the corresponding FA images obtained immediately after acquiring color fundus images shown in Figure 2a–g.

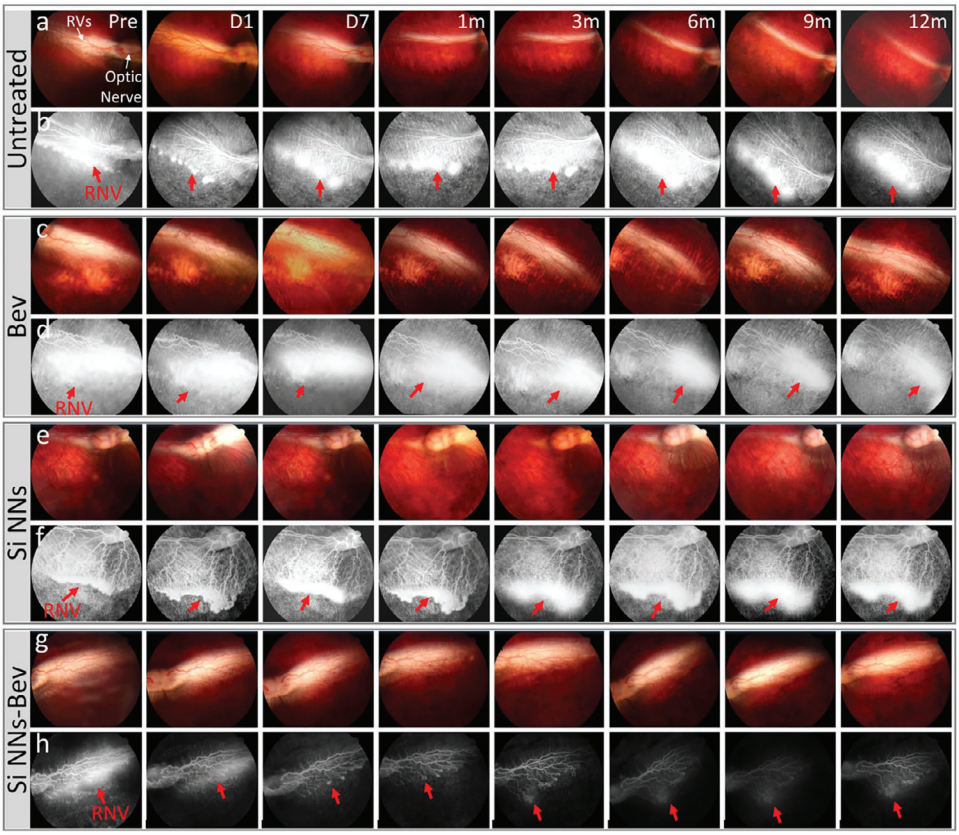

Figure 2. In vivo treatment of RNV in rabbits using Si NNs: a,c,e,g) Color fundus photographs captured at various time points over a 12-month post-treatment period, representing four groups: the untreated control group (a), the group treated with Bev alone (c), the group treated with Si NNs without Bev (e), and the group treated with Si NNs conjugated with Bev (Si NNs-Bev, g). These images clearly illustrate the RV structure and the optic nerve. b,d,f,h) Corresponding FA images acquired after the color fundus photographs in panels a, c, e, and g. The FA images provide high-resolution views of the RNV structure, with leakage areas indicative of new RNV development highlighted by red arrows. Notably, the FA images demonstrate that the Si NNs-Bev treatment effect decreased over time, whereas the untreated control, Bev-only, and Si NNs groups showed minimal regression of RNV.

Significant reductions in RNV were observed following Si NNs-Bev treatment (Figure 2h; Figure S1h, Supporting Information), while minimal changes were noted in the control or untreated group (Figure 2b; Figure S1b, Supporting Information), treated with Bev (Figure 2d; Figure S1d, Supporting Information), and treated with Si NNs (Figure 2f; Figure S1f, Supporting Information). This suggests the efficacy of Si NNs-Bev patch in attenuating RNV progression over an extended period, highlighting its potential as a therapeutic intervention for retinal neovascularization.

To quantify both the density of RNV and the fluorescent intensity (FLI) observed in the FA images, we employed image segmentation (Figure S2, Supporting Information). Following the segmentation of RNV locations, we determined RNV density and FLI using ImageJ, as depicted in **Figure 3**. The FLI of RNV gradually decreased after treatment, reaching its lowest point at 4 months before a slight increase between months 5 and 12 (Figure 3a). Compared to pre-treatment levels, the normalized FLI decreased by ≈85% (Nor_{FLI} = 1±0.01 (a.u.) pre-treatment versus 0.15±0.06 (a.u.) post-treatment at month 6). This result illustrates the long-term impact of the Si NNs-Bev on RNV progression and vascular leakage, consistent with drug release from the Si NNs, as demonstrated in our previous publication.[22] Conversely, the control groups such as untreated or Si NNs without Bev treatment showed ongoing RNV growth after 1 month, with a slight reduction ≈2–3% compared with pre-treatment between months 1 and 4, followed by no change up to 12 months. In the group treated with Bev, we observed a 7% reduction in RNV during the first month after administration. This reduction continued, reaching 10–13%, and remained stable for up to 12 months post-treatment (Nor_{FLI} = 1±0.01 (a.u.) pre-treatment versus 0.88±0.05 (a.u.) post-treatment at month 10).

Figure 3b illustrates the quantification of RNV density as a function of treatment time. RNV density decreased rapidly after the Si NNs-Bev treatment, achieving an 85% reduction compared to pre-treatment levels (RNV density = 1.00±0.00 (a.u.) pre-treatment versus 0.15±0.02 (a.u.) post-treatment at month 6). In contrast, RNV density increased by ≈9% in the untreated group (RNV density = 1.00±00 (a.u.) pre-treatment versus 11.11±0.28 (a.u.) post-treatment at month 4) and then increased by 4% and 2% at month 8 and 12 (RNV density = 0.97±0.17(a.u.) post-treatment at month 8 and 0.98±0.02 (a.u.) post-treatment at month 12), respectively. Similarly, the groups treated with Bev and Si NNs exhibited slight fluctuations in VD compared to their pre-treatment levels. Measurements indicated that RNV density decreased by 7% in the Bev-treated group at month 6 while the Si

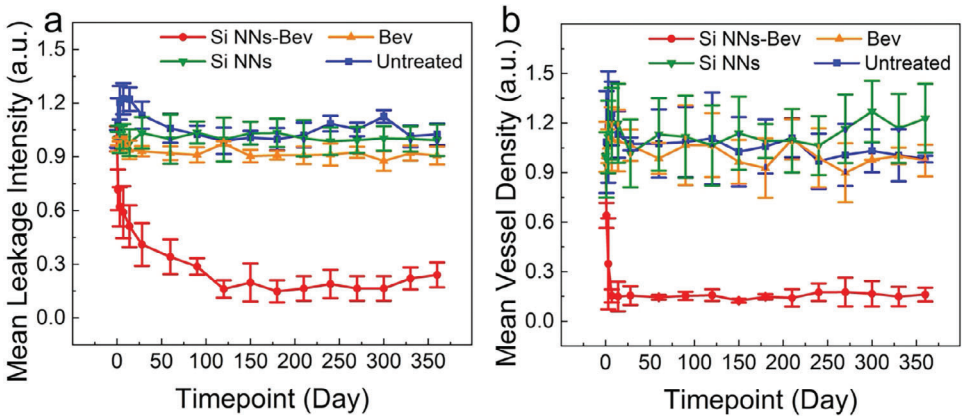

Figure 3. Measurement of fluorescent intensity and vessel density: a) Normalized fluorescent leakage intensity. The blue line represents the trend observed in the control group (untreated), the orange line depicts the signal resulting from intravitreal Bev treatment, and the green line shows the quantified data from the group treated with Si NNs alone while the red line depicts the progression of the Si NNs-Bev treatment. b) Vessel density measurement over time. Data are presented as Mean±Standard Deviation with N = 3.

NNs-treated group demonstrated RNV increased by 9% at month 6 and fluctuated ≈22% at month 12.

2.3. In Vivo OCT Imaging for Monitoring RNV Treatment with Si NNs Patch

Next, the efficacy of the Si NNs-Bev treatment in managing RNV was assessed through high-resolution spectral domain (SD)-OCT imaging. OCT imaging provided high-resolution cross-sectional views of the retina, enabling a detailed assessment of RNV progression and regression over the treatment period. The margin and degree of retinal neovascularization (RNV) were visualized both in 2D and 3D OCT, offering a comprehensive understanding of the morphological changes in RNV pre- and post-treatment (**Figure 4**). The selected images obtained from the control group (Figure 4a–e) offered a detailed depiction of the distribution of newly developed RNV and stable up to 12 months with high resolution following treatment. These images not only highlighted the presence of RNV, but also provided clarity regarding other retinal layers such as choroidal vessels (CVs) and sclera, thus enriching our understanding of the retinal microenvironment. In contrast, the treated group with the Si NNs-Bev (Figure 4f–j) demonstrated a significant reduction in RNV density as early as 1-month post-treatment (Figure 4g), with sustained suppression observed throughout the 12-month follow-up period (Figure 4j). This reduction in RNV density highlights the therapeutic potential of the Si NNs-Bev in mitigating pathological neovascularization within the retina.

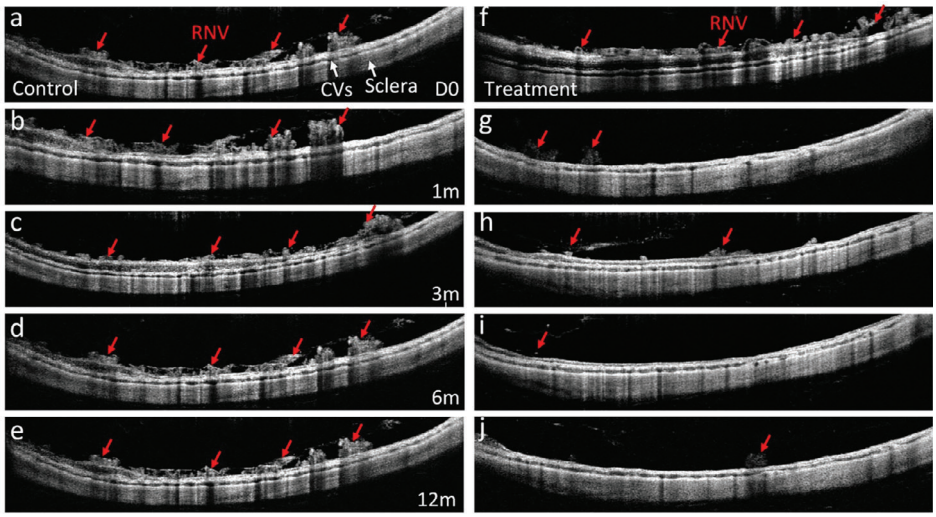

Figure 4. In vivo OCT monitoring of retinal neovascularization (RNV) progression following treatment with the Si NNs: a–e) Two-dimensional OCT images captured from the control group, untreated with the Si NNs-Bev, prior to treatment (a) and post-treatment at varying time intervals: 1 month (b), 3 months (c), 6 months (d), and 12 months (e). The red arrows denote the sites of newly developed RNV resulting from intravitreal injection of DL-alpha-aminoadipic acid (DL-AAA). f–j) OCT images acquired from the Si NNs-Bev treated group at different time points: pre-treatment (f), 1 month (g), 3 months (h), and 12 months (j). RNV density gradually diminishes post-treatment, commencing at 1 month, with minimal recurrence observed up to 12 months.

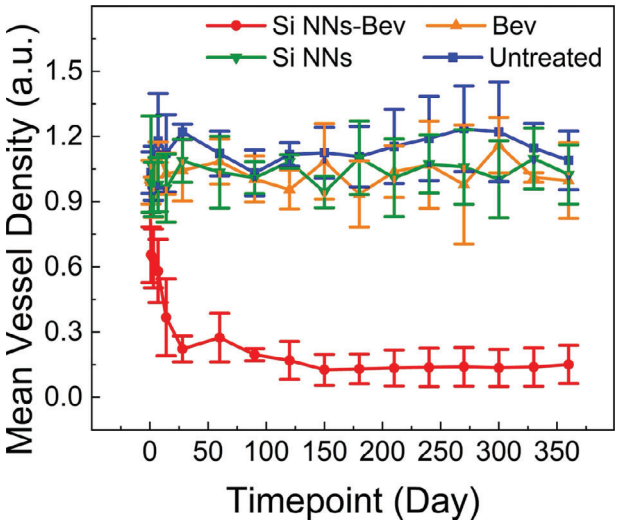

Figure 5. Quantification of vessels density as a function of treatment time. The graph depicts the changes in RNV density across treatment groups: blue represents the untreated group, orange corresponds to Bev-treated, green indicates Si NNs-treated, and red denotes Si NNs-Bev-treated. A significant reduction in RNV density was observed in the Si NNs-Bev group, while only minimal reductions were detected in the other groups. Data are presented as Mean±Standard Deviation with N = 3.

The quantitative analysis presented in **Figure 5** further supports these observations, with the Si NNs-Bev-treated group exhibiting an impressive 87% reduction in RNV density compared to pre-treatment levels by 6 months that persists to 12 months (VD = 1.00±0.01 (a.u.) for pre-treatment versus 0.15±0.09 (a.u.) for post-treatment with the Si NNs-Bev at 12 months). This significant decrease in vessel density underscores the efficacy of the Si NNs-Bev in inhibiting RNV progression and highlights its promise as a therapeutic intervention for neovascular retinal disorders. Moreover, there was no significant reduction in RNV density observed in the untreated, Si NNs, and Bev groups (VD = 1.00±0.01 (a.u.) for pre-treatment versus 1.09±0.13 (a.u.), 1.03±0.14 (a.u.), and 1.00±0.17 (a.u.) for post-treatment at 12 months, respectively).

2.4. In Vivo Photoacoustic Microscopy Visualization of RNV after Treatment with Si NNs

To further investigate the development of RNV in three dimensions (3D), we conducted photoacoustic microscopy (PAM) imaging. PAM imaging utilized an excitation wavelength of 578 nm, chosen for its strong optical absorption by hemoglobin in the vessels,[29,30] as depicted in **Figure 6**. In both the control and Si NNs-Bev-treated groups, the morphology of RVs was clearly visualized using fundus imaging (Figure 6a,d), red-free imaging (Figure 6b–e), and FA (Figure 6c,f). Notably, minimal FA leakage was observed in the Si NNs-Bev-treated group (Figure 6f), while a strong FA leakage signal was detected in the control group (Figure 6c). These findings confirm the effectiveness of the Si NNs-Bev treatment. Figure 6g–i shows the PAM images of RNV from the control group at various time points: Pre-treatment (g), 1-month post-treatment (h), and 12-months post-treatment (i) obtained along the scanning region showed in Figure 6a. The morphology of RNV was distinctly discernible, characterized by high resolution and image contrast. Additionally, PAM images revealed detected retinal pigment epithelium (RPE) cells exhibiting strong photoacoustic signals. Figure 6m–o depicts the 3D volumetric rendering of PAM data, offering an impressive structural depiction of RNV in a 3D perspective. Notably, the RNV and RPE layers were distinctly visualized at different depths, consistent with the layering observed in the OCT images presented in Figure 5 (Videos S1–S3, Supporting Information). Figure 6j–l presents the PAM images acquired from the group treated with Si NNs-Bev acquired along the scanning region shown in Figure 6d–f. A detailed depiction of the RV structure is evident in the PAM image captured at 1, 6, and 12 months. Note that a reduced RNV population without recurrence is observed in the Si NN-Bev treated group when compared to the control group (Figure 6h,i), indicative of the therapeutic effect of the Si NNs-Bev. The 3D reconstructions of PAM images are displayed in Figure 6p–r. These reconstructions demonstrate the RV structure post-treatment, featuring diminished microvasculature compared to pre-treatment (Videos S4–S6, Supporting Information). Furthermore, a reduction in vessel tortuosity is evident in the post-treatment PAM images. In addition, the RNV and RPE layers were located at different layers, which is consistent with the OCT images presented in Figure 5.

2.5. Grimace Scale and Biosafety Analysis

To assess the comfort of the animals after treatment with the Si NNs, we performed a grimace scale analysis (Figure S3, Supporting Information). No signs of discomfort were observed in any of the treated rabbits, including the control group. This indicates that the Si NNs are both painless and safe for treatment. To evaluate the safety of the Si NNs treatment for RNV, a comprehensive in vivo biosafety assessment was conducted on all treated animals. Monthly observations of body weight were performed on all treated animals, including the control group, post-treatment (**Figure 7a**). The data indicate a uniform, gradual increase in body weight across all groups, suggesting that the treatment did not adversely affect the health of the rabbits. To corroborate the presence of RNV, animals were euthanized at 12 months post-treatment for histological analysis. Figure 7b–e displays hematoxylin and eosin (H&E) staining of the Si NNs-Bev treated group (b), Bev treatment (c), Si NNs treatment (d), and the control group without treatment (e). The control groups exhibit a clear structure and morphology of RNV, along with major RVs, while the treated group with Si NNs-Bev displays fewer structures of RVs. This observation is consistent with findings from OCT, PAM, and FA imaging. Furthermore, in the treated group with the Si NNs-Bev, no evidence of residual Si NNs was observed. This suggests that the Si NNs can be completely degraded and therefore can be applied repeatedly. Further biosafety analysis was conducted using TUNEL staining to assess the potential toxicity of the Si NNs to the retina. As shown in **Figure 8**, no TUNEL-positive cells were detected in either the treated groups or the control group, indicating that the treatment caused minimal toxicity to the retinal tissue.

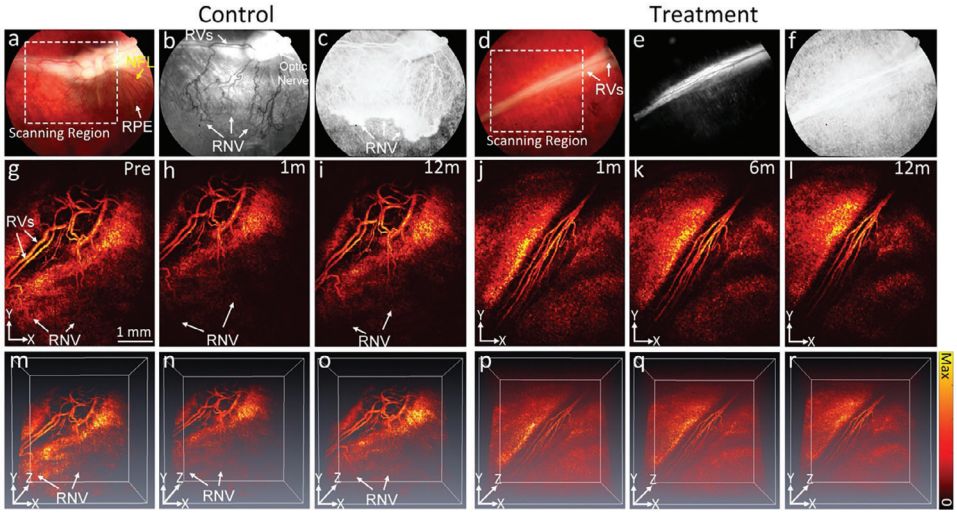

Figure 6. In vivo PAM imaging visualization of retinal neovascularization (RNV). a,d) Color fundus photography showing the major RVs and RPE before treatment obtained from control (a) and treated group with Si NNs-Bev (d). b,e) Red-free image highlighting the nerve fiber layer (NFL), RVs, and areas of RNV. c,f) Late-phase FA image illustrating retinal neovascularization (RNV) and the detailed structure of RVs and capillaries. g–i) PAM images taken before treatment (g), at 1 month (h), and at 12 months (i), corresponding to the scanned area outlined by the white dotted rectangle in (a), providing a high-resolution view of RVs and RNV. j–l) PAM images achieved from treated group Si NNs-Bev at different time points, showing minimal newly developed RNV. m–r) 3D volumetric reconstruction PAM images depict the morphology of RVs and RNV in a 3D perspective.

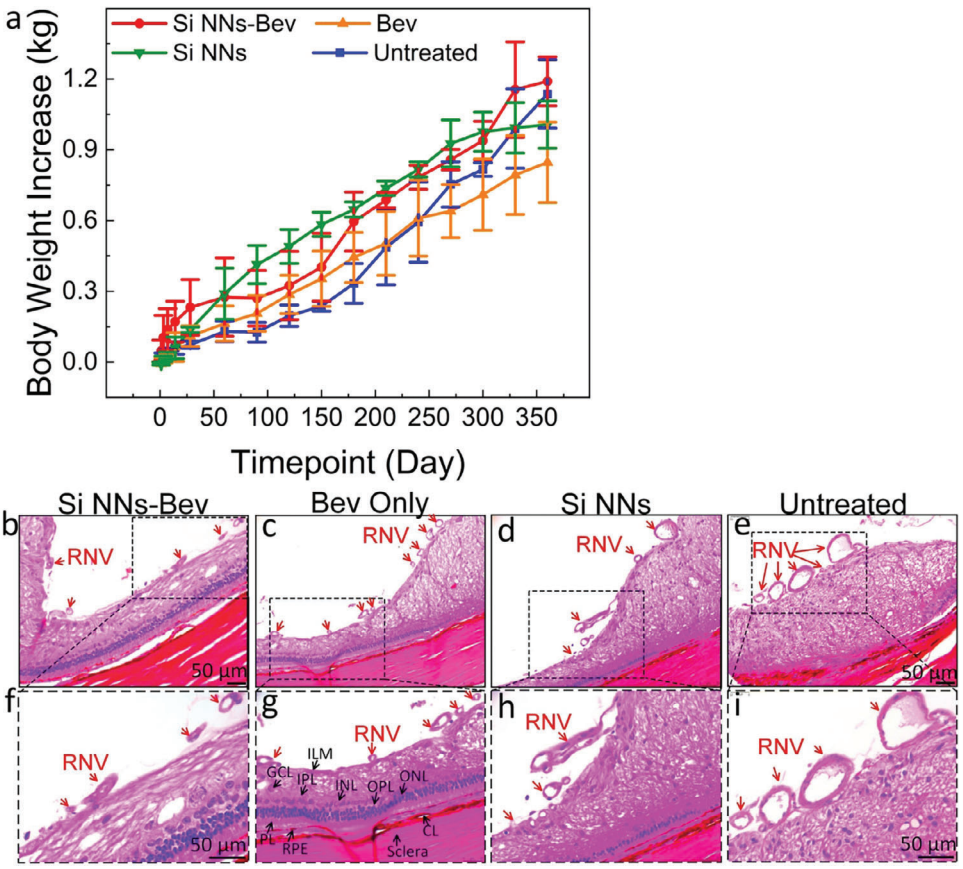

Figure 7. In vivo biosafety analysis. a) Body weight of the rabbits monitored before and followed up for 12 months post-treatment with Si NNs-Bev, Bev, Si NNs, and control (untreated). b–e) 20x H&E images obtained from Si NNs-Bev treatment (a), Bev treatment only (c), and Si NNs treatment (d) and untreated group (e). f–i) 40x H&E images from (b–e) respectively. These images show clearly the location of RNV (red arrows). In addition, the architecture of the retinal layers was also observed clearly, such as ILM, ganglion cell layer (GCL), inner plexiform layer (IPL), inner nuclear layer (INL), outer plexiform layer (OPL), outer nuclear layer (ONL), photoreceptor layer (PL), RPE, choroid layer (CL), and sclera.

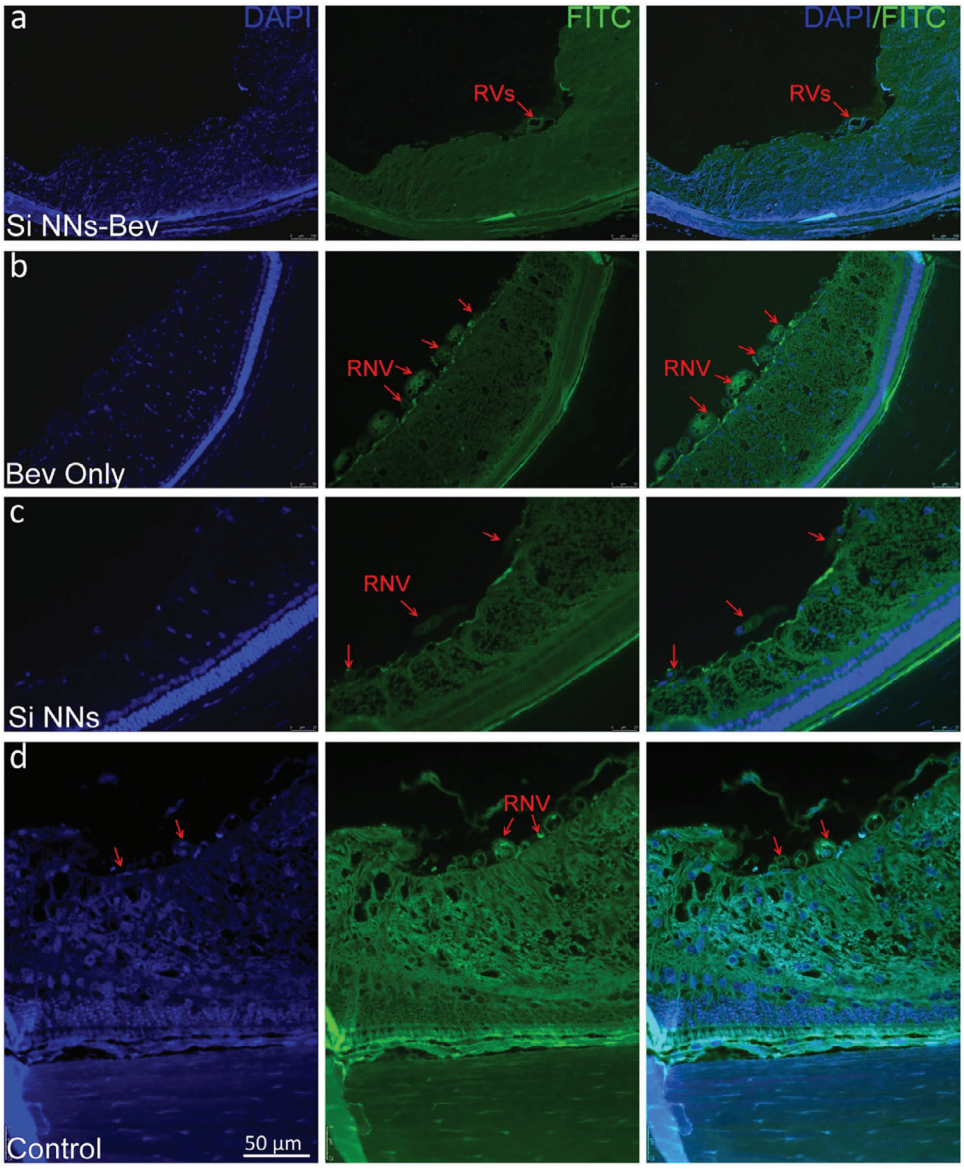

Figure 8. TUNEL assay analysis 12 months after Si NNs-Bev treatment. a) Si NNs-Bev treated group. b) Bev treated group. c) a group treated with Si NNs without conjugation with Bev. d) Control group (untreated). Cell nuclei are stained with DAPI (blue), while apoptotic cells are stained with FITC (green). No evidence of apoptotic cells was detected in any of the groups. Scale bar: 50 µm.

2.6. Immunofluorescence Analysis

We then performed immunofluorescence imaging (IF) to confirm the presence of newly developed retinal blood vessels and assess the treatment's effectiveness. **Figure 9** displays IF images of the retina stained with α-SMA and CD31 antibodies from different treatment groups: Si NNs-Bev treated, Bev only treated, Si NNs without conjugation with Bev, and control or untreated. In these images, α-SMA antibody was used to label the vessel walls. This antibody showed strong expression on the walls of major arteries and capillaries in the Bev-only treated group (Figure 9b), Si NNs (Figure 9c) and the control group (Figure 9d) but was less expressed in the Si NNs-Bev treated group (Figure 9a). These results indicate that RNV was almost completely resolved after treatment with the Si NNs-Bev, whereas new blood vessels remained in the control groups. The CD31 antibody was primarily expressed on the lumen of the vessel walls.

3. Discussions

The utilization of the Si NNs conjugated with Bev for long-term treatment of RNV in a DR rabbit model has shown promising outcomes. Our study has demonstrated a novel treatment approach utilizing a biodegradable subconjunctival patch with the Si NNs embedded in the sclera, representing a significant advancement in drug delivery for long lasting ocular therapeutics. This innovative method offers several key advantages including minimal invasiveness, reduced patient discomfort, long term

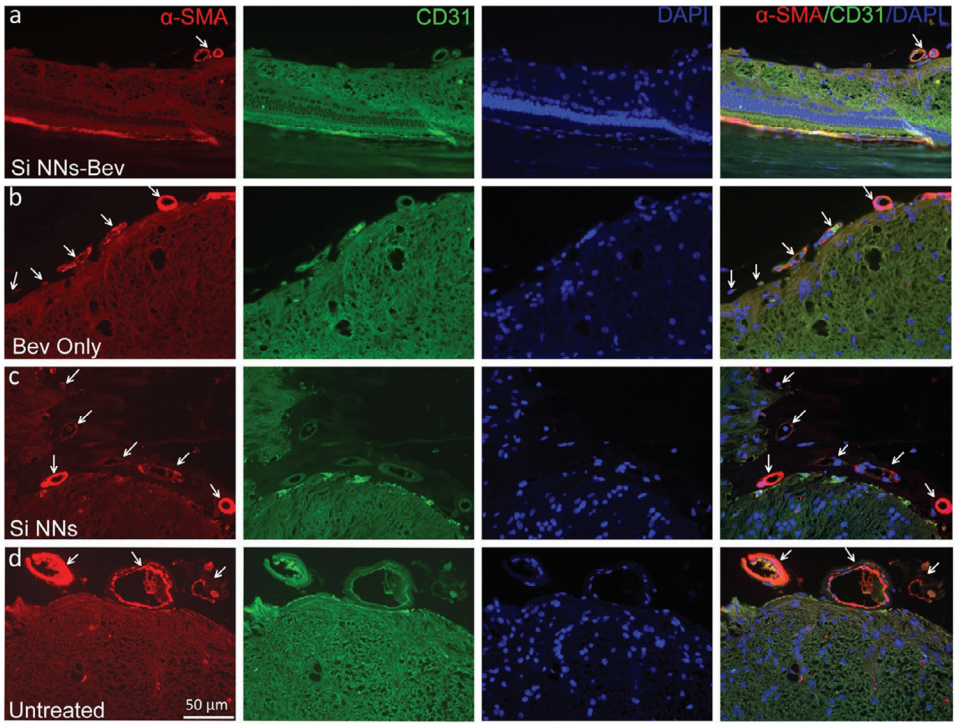

Figure 9. Immunofluorescent analysis of RNV after treatment with Si NNs. a–d) Fluorescence images of the retina stained with different vascular markers: α-SMA (red), and CD31 (green). Blue fluorescent color indicates the distribution of cell nuclei stained with DAPI. The images show the results from the group treated with Si NNs-Bev (a), the group treated with Bev alone (b), the group treated with Si NNs without Bev and the untreated group (d). White arrows indicate the locations of vascular walls labeled with α-SMA.

sustained drug delivery, and enhanced effectiveness in drug delivery.

The use of a subconjunctival patch with the Si NNs embedded in the sclera minimizes the need for invasive procedures such as intravitreal injections, which are associated with discomfort and potential complications such as infection or retinal detachment.[31,32] The biodegradable nature of the patch allows release of the drug in a controlled manner, ensuring sustained local therapeutic levels while minimizing systemic exposure and potential side effects. This controlled release mechanism enhances the efficiency of drug delivery, prolonging the duration of therapeutic action, and reducing the frequency of administration required.

The subconjunctival route of administration with the Si NNs embedded in the sclera also offers unique benefits in terms of drug distribution and targeting. By placing the patch in close proximity to the target tissues, it allows for efficient diffusion of the therapeutic agent in the sclera and adjacent retina, where it can exert its pharmacological effects. This localized delivery approach enhances the therapeutic index of the drug, maximizing its efficacy while minimizing off-target effects on nonocular tissues. Throughout the 12-month post-treatment period, the efficacy of this therapeutic approach was monitored using various imaging modalities including color fundus photography, FA, OCT, and photoacoustic microscopy (PAM) imaging. The findings indicate a significant, sustained > 80% reduction in RNV and vascular leakage following treatment, coupled with minimal recurrence observed over the duration of the study. This notable reduction in RNV and vascular leakage suggests that the Si NNs-Bev effectively targeted and inhibited the pathological angiogenesis characteristic of RNV in the diabetic rabbit model.

The major advantage of this study is that we monitored RNV post-treatment using different imaging modalities longitudinally for a long one-year time period, which allowed us to thoroughly observe RNV progression over time. Color fundus imaging provided valuable insight into the macroscopic changes occurring in the retina, allowing for the visualization of vascular abnormalities and alterations in retinal morphology. The observed reduction in RNV on color fundus images corroborates the efficacy of the Si NNs-Bev treatment regimen. FA served as a crucial tool for assessing retinal vascular perfusion and leakage, enabling the visualization of abnormal neovascularization and the extent of vascular regression post-treatment. The decrease in fluorescein leakage and neovascularization observed in treated rabbits further supports the therapeutic efficacy of the Si NNs-Bev in treating RNV.

OCT imaging provided detailed cross-sectional visualization of retinal layers and structural changes, allowing for the assessment of morphological alterations and the presence of fluid accumulation. The reduction in RNV density and absence of significant fluid accumulation observed on OCT images also validate the effectiveness of the Si NNs-Bev in stabilizing retinal morphology and function. PAM offered additional insights into the 3D structure of RNV and provided complementary information regarding vascular architecture and microvascular changes. The 3D reconstruction of photoacoustic images demonstrated a clear

reduction in microvasculature and vessel tortuosity post-treatment, consistent with the findings from other imaging modalities. Therefore, the combined use of the Si NNs conjugated with bevacizumab for the long-term treatment of RNV in a DR rabbit model yielded promising results, as evidenced by the significant and sustained reduction in RNV with minimal recurrence observed over the 12-month treatment period. These findings highlight the potential of this therapeutic approach for the management of RNV in DR and highlight the importance of multimodal imaging in assessing treatment efficacy and disease progression.

While the Si NNs show promise in treating RNV through scleral embedding, several challenges must be addressed to enhance their effective implementation. The efficient delivery of the Si NNs to the target site within the retina is crucial for therapeutic efficacy. Subconjunctival administration with the Si NNs embedded in the sclera may face barriers in achieving adequate penetration and distribution of the Si NNs to the retinal layers where neovascularization occurs. In addition, achieving sustained release of therapeutic agents, such as bevacizumab, from the Si NNs is essential for prolonged therapeutic effect. Maintaining optimal drug concentration levels over time while minimizing systemic exposure is also a challenge. The efficient loading of therapeutic agents in the Si NNs is crucial for enhancing their effectiveness in the treatment of RNV. Several promising methods can address this challenge, including the utilization of longer Si NNs. In our current study, we employed 60 µm in length Si NNs(*22*). If needed, to increase drug delivery into the retina, one could explore increasing the length of Si NNs to 150–200 µm. This longer length may help facilitate enhanced drug loading and subsequent release, although in this study 60 µm in length was able to achieve treatment efficacy for RNV. Additionally, microneedles offer another promising avenue for ocular drug delivery[33,34] and have shown potential in the treatment of various ocular diseases such as glaucoma, AMD, uveitis, retinal vascular occlusion, and retinitis pigmentosa,[35,36] demonstrating potential applications beyond traditional delivery routes. Recent investigations have explored diverse sizes and shapes of microneedles, highlighting their adaptability to specific therapeutic needs. While microneedles hold great promise for inhibiting neovascular proliferation, challenges and potential side effects must be addressed to facilitate their widespread application, including tissue penetration, biocompatibility, and potential adverse reactions. Nonetheless, continued research and development efforts in optimizing microneedle technology offer exciting prospects for enhancing the efficacy and safety of retinal treatments, including the management of RNV.

However, subconjunctival administration with Si NNs embedded in the sclera may face challenges in achieving sufficient penetration to the retina, especially in cases of thickened or fibrotic scleral or subretinal tissue. Therefore, alternative methods to enhance tissue penetration while minimizing trauma to ocular structures would be beneficial.

4. Conclusion

This study demonstrates the feasibility and efficacy of utilizing a rapidly dissolving subconjunctival patch with Si NNs embedded in the sclera for ocular drug delivery. This approach represents a promising alternative to traditional treatment modalities, offering enhanced comfort, improved treatment outcomes, greater convenience, and long-term, sustained drug delivery. Further research and development in this area hold the potential to revolutionize the field of ocular therapeutics, providing safer, more effective treatment options for a wide range of ocular diseases and conditions.

5. Experimental Section

Fabrication of Si NNs on Si Wafer: The fabrication process for the silicon nanoneedles (Si NNs) patch began with the formation of vertically aligned arrays of microscale silicon pillars (initial height/diameter: ≈65/2 µm) on a bulk silicon wafer (p-type; 525 µm thick; 0 to 100 ohm·cm). This was accomplished using conventional photolithographic patterning followed by a deep reactive ion etching (DRIE) process. The DRIE was conducted under specific parameters: a radio frequency (RF) plasma power of 450 W and a platen power of 11 W, with sulfur hexafluoride (SF_6) gas flowing at 85 sccm. A partial passivation layer of $(C_xF_y)_n$ polymer was then deposited using octafluorocyclobutane (C_4F_8) gas at a flow rate of 130 sccm under an RF plasma power of 800 W. This step aimed to create Si micropillars with precise vertical alignment and an optimal aspect ratio. Subsequently, an additional isotropic dry etching was performed using a plasma power of 450 W and a platen power of 30 W, with SF_6 gas at a flow rate of 85 sccm, to generate undercuts at the base of the Si micropillars. To remove residues such as photoresist and passivation layers generated during the DRIE process, the specimen underwent treatment with oxygen (O_2) plasma and piranha solution (80% sulfuric acid [H_2SO_4] and 20% hydrogen peroxide [H_2O_2]). The Si micropillars were then immersed overnight in phosphate-buffered saline (PBS; pH 7.4) at 67 °C, followed by a 10-min immersion in a 15 wt.% potassium hydroxide (KOH) solution at 25 °C to reduce the size of the Si micropillars from microscale to nanoscale, forming the Si NNs. Next, a metal-assisted chemical etching (MACE) process was applied, where the pillars were immersed in a mixture of 20 mM silver nitrate ($AgNO_3$) and 49% hydrogen fluoride (HF) to create a nanoporous surface. Silver residues were then removed immediately using an Ag etchant solution for one minute. Finally, a thin film of aluminum oxide (Al_2O_3) was deposited by atomic layer deposition (ALD), with each cycle designed to deposit 1 Å of thickness, for a total of 30 cycles. The resulting Si NNs in this study had a base diameter of 900 nm and a length of 65 µm.

Transfer Printing of Si NNs onto Biodegradable Patch: A 200 µm thick layer of PMMA film was spin-coated onto the surface of the as-prepared Si NNs on a silicon wafer, followed by thermal curing in a vacuum chamber at 80 °C for 2 h. This process created an air gap of ≈5 µm between the PMMA layer and the Si wafer, due to surface tension effects. The PMMA film was then mechanically peeled off at a constant rate of 50 mm/min using a Mark-10 device from Willrich Precision Instruments. A 500 µL volume of PVA solution (molecular weight = 31000; 2 wt.%) was drop-cast onto the side of the PMMA film where the Si NNs were exposed, followed by curing in a vacuum chamber at 60 °C for one hour. To achieve a PVA film thickness of 40 µm, this step was repeated three times under identical conditions. The resulting double-layered PMMA-PVA structure was then immersed in acetone at 70 °C for 4 h to selectively dissolve the PMMA layer. For sterilization, the biodegradable patch with embedded Si NNs was soaked in an anhydrous ethanol bath for 5 min and subsequently exposed to ultraviolet (UV) light at a wavelength of 254 nm for 5 min before each use. The biodegradable subconjunctival patch used in this study is 1.5 cm by 1.5 cm square, accommodating ≈5000 Si NNs per square centimeter, with each nanoneedle measuring 60 µm in length.

Drug Loading Process: To achieve covalent bonding between Si NNs and Bev, 500 µL of TESPSA was applied to Si NNs at room temperature for 10 min to functionalize the surface with silane, followed by rinsing with anhydrous ethanol. For the loading of Bev to Si NNs, the Bev solution was prepared by diluting it to 5% (v/v) in anhydrous ethanol (≥99.9%). The Si

NNs were immersed in this solution at room temperature for 30 min and then washed with anhydrous ethanol.

Animal Preparation: All animal experiments were employed under the ARVO (The Association for Research in Vision and Ophthalmology) guideline for the Use of Animals in Ophthalmic and Vision Research and the protocol was approved by the Institutional Animal Care & Use Committee (IACUC) of the University of Michigan (Protocol PRO00010388, PI: Y.M. Paulus). Adult Dutch Belted pigmented rabbits, both genders, and weight of 2.3–2.7 kg, age 4–8 months old were used in this study. Ketamine (40 mg k^{-1}g) and xylazine (5 mg k^{-1}g) were applied for anesthesia through intramuscular administration. To maintain anesthesia, one third dose of ketamine was administered during the experiment every 45 min. The animal's pupil was dilated using phenylephrine hydrochloride 2.5% and tropicamide 1% ophthalmic solution. The rabbit's eyes received a drop of topical tetracaine for topical anesthesia. The animal vitals, including such as heart rate, respiratory rate, mucous membrane color, and body temperature, were monitored and documented every 15 min during anesthesia and recovery. The heart rate and respiratory rate were measured using a SpO2 Digital Pulse Oximetry (V8400D, MWI Animal, Health, Boise, ID). To maintain the body temperature, a water circulation blanket was used during the experiment (TP-700, Stryker Corporation, Kalamazoo, MI). In addition, a balanced salt solution was applied on the eye every minute to prevent corneal dehydration (Altaire Pharmaceuticals, Inc., Aquebogue, NY).

In Vivo OCT-PAM Imaging: The response to Si NNs treatment was evaluated using a combination of imaging techniques, including a dual SD-OCT and photoacoustic microscopy (PAM) system.[37–44] The SD-OCT system utilized in this research was a modified version of the Ganymede-II-HR system by Thorlabs (Newton, NJ, USA), incorporating additional components such as an ocular lens, scan lens, and dispersion compensation glass (DCG). An optical parametric oscillator (OPO) served as the light source for PAM (Model NT-242, Ekspla, pulse duration of 3–5 ns, with tunable wavelength ranging from 405 nm to 2600 nm). Last, a custom ultrasonic transducer from Optosonic Inc (Arcadia, CA, USA) was employed to capture the photoacoustic (PA) signal generated by the excitation of chromophores such as hemoglobin. This transducer has the center frequency of 27 MHz. The signal underwent digitization using a high-speed digitizer with a sampling rate of 200 MS/s (PX1500-4, Signatec Inc., Newport Beach, CA, USA) and was then amplified utilizing a low-noise amplifier (with a gain of 57 dB, AU-1647, L3 Narda-MITEQ, NY, USA). For PAM and SD-OCT, the lateral resolutions are 4.1 µm and 3.8 µm respectively, with an achievable imaging depth of 1.9 mm. The center laser wavelength for the OCT system was 905 nm, employing two super luminescent light-emitting diodes with center wavelengths of 845 nm and 932 nm. The laser energy was maintained at half of the ANSI safety limit, ≈80 nJ.

Fundus and Fluorescein Angiography Imaging of RNV: A custom-modified 50° color photography system (Model Topcon 50EX, Topcon Corporation, Tokyo, Japan) was utilized for visualizing the RNV changes in response to treatment. Photographs were captured on an Electro-Optical System (EOS) 5D camera (Cannon 5D EOS, Tokyo, Japan) with a resolution of 5472 × 3648 pixels, each pixel measuring 6.55 μm^2. Red-free photography and FA images were acquired using the same Topcon 50EX camera with appropriate filters and internal excitation. FA images were acquired serially immediately after intravenous injection of fluorescein solution (200 µL, 100 mg mL^{-1}) up to 15 min post injection. Additionally, the picture style was set to monochrome to enhance the visualization of new blood vessels. The red-free image provided high signal contrast for the vasculature, facilitating the quantitative analysis of dynamic changes in RNV over time.

Diabetes Retinopathy Model: To create a clinically-relevant model of DR in rabbits, the DL-alpha-aminoadipic acid (DL-AAA) model was utilized in pigmented rabbits as published previously.[45,46] Briefly, DL-AAA stock solution (120 mg mL^{-1}) was prepared by dissolving DL-AAA powder obtained from Sigma (Sigma-Aldrich, USA) in 1N hydrochloric acid. The pH level was adjusted to 7.4 using sodium hydroxide solution. Then, the stock solution was diluted in PBS to achieve final concentration of 80 mM. Before injection, the mixed solution was filtered using a 0.22 µm disposable syringe filter (Millex-GP, MKBL8989, Sigma-Aldrich Corp.). All animals received intravitreal injection (IV) of 50 µL DL-AAA into the vitreous cavity using a 30 G ½ inch insulin syringe through the pars plana at 3.5 mm posterior to the corneal limbus. To avoid reflux, a cotton swap was applied at the injection area immediately after withdrawal of the needle.

RNV Treatment Procedure: To perform RNV treatment, we divided the rabbit models into four groups: a control group (no treatment with Si NNs), a group treated with bevacizumab only (Bev only), a group treated with Si NNs without bevacizumab (Si NNs only), and a group treated with Si NNs conjugated with bevacizumab (Si NNs-Bev). In the control group, no surgery was performed after the creation of the RNV model, serving as a baseline for evaluating the effects of the Si NNs and Si NNs-Bev treatments. For the group treated with bevacizumab only (Bev only), intravitreal injection was performed to deliver bevacizumab directly into the vitreous using a 30G ½ insulin syringe to mimic the standard clinical treatment of DR. For the other groups, we administered subconjunctival treatment using Si NNs embedded in the sclera for the DL-AAA-induced RNV model in rabbits. To do this, a localized quadrant sectoral peritomy was performed using Westcott scissors (Figure S4, Supporting Information). Then, Si NNs patches were inserted through this localized peritomy. Artificial lubricant eye drops (Systane, Alcon, TX, USA) were added to the cornea to prevent dehydration and to improve the dissolution of the patch. The patch completely dissolved within 1 min post application (Video S7, Supporting Information). The RNV progression was monitored before and after Si NNs treatment up to 12 months using multimodal imaging.

Grimace Scale Evaluation: To assess the comfort of the animals after treatment with a subconjunctival patch, a grimace scale evaluation was performed.[47] Digital images of the animals' faces were taken before and after treatment, and these images were analyzed to identify any signs of discomfort. Key facial features such as the shape of the nose (specifically the V-shape), orbital tightening, cheek flattening, ear shape and orientation, and whisker shape and position were carefully observed to identify signs of discomfort. The grimace scale is a reliable and non-invasive tool for measuring pain and discomfort in animals, as it quantifies specific facial expressions that correlate with distress. This evaluation is crucial in determining the effectiveness of the treatment and ensuring the well-being of the animals.

In Vivo Biosafety Evaluation: Comprehensive biosafety evaluation was performed on all the treated groups including control group using body weight analysis, standard H&E, and TUNEL assay. The weight of the animal was measured before and every day after treatment for up to 1 week and once a week from the second week up to 12 months. The trend of body weight was plotted using Origin software. To perform H&E analysis, all animals were euthanized after 12 months, and the eye tissues were collected for H&E staining. To avoid retinal detachment, the harvested tissues were pre-fixed in Davidson's fixative solution (Fisher Scientific, MD, USA) for 24 h. Afterward, the samples were changed to 50% alcohol for 8 h and then preserved in 70% alcohol for 24 h until sectioning. The eyeballs were sectioned into two halves at the center of the optic nerves. The half eyeball containing the treated area was embedded in paraffin. The paraffin-embedded sections with a thickness of 5 µm were acquired using microtome equipment and stained with H&E. The stained sections were evaluated under Leica Microscope (DM6000, Leica, USA). Digital images were captured using a DF450C camera (Leica Microsystems Inc., IL, USA).

TUNEL Assay Analysis: To assess the potential toxicity of Si NNs on retinal tissue, a TUNEL assay was conducted following the TUNEL in situ Cell Death Detection Kit protocol (Sigma-Aldrich, USA). The TUNEL protocol involves detecting apoptotic cells by labeling DNA strand breaks with fluorescently labeled nucleotides. First, tissue sections or cell samples are fixed and permeabilized to allow the reagents to penetrate the cells. The samples are then incubated with a reaction mixture containing terminal deoxynucleotidyl transferase (TdT) enzyme, which catalyzes the addition of labeled nucleotides to the 3′-OH ends of fragmented DNA. After incubation, the samples are washed to remove unincorporated nucleotides. Finally, the labeled cells are visualized under a fluorescence microscope, where apoptotic cells will exhibit bright fluorescence, indicating DNA fragmentation.

Immunofluorescent Analysis: Immunofluorescence staining was conducted to validate the emergence of RNV. Paraffin-embedded slides were

first immersed in 4% PFA for 15 min at room temperature, followed by a wash with 1% saponin in PBS for 30 min at room temperature to facilitate permeabilization. Subsequently, the slides were incubated overnight at 4 °C in a solution containing 1% BSA, 10% goat serum in PBS. Two primary antibodies CD31(P8590, Sigma Aldrich, USA) and mouse anti alpha smooth muscle Actin (αSMA) (A2547, Sigma Aldrich, MA, USA) were ordering applied at a dilution of 1:1000 in blocking buffer and incubated overnight at 4 °C. Finally, the samples were washed with 0.1 M PB (pH 7.4) and a secondary antibody, Alexa FluorTM 488-conjugated goat anti-rabbit IgG (A11008, Thermos Fisher, MD, USA), was applied at a dilution of 1:500 in blocking buffer and incubated for an additional 2 h at room temperature in the dark. After that, the samples were washed with 0.1 M PB and coverslipped with prolong gold antifade mountant with DNA stain DAPI (P36941, Invitrogen, MA, USA). Microscopic examination of the slides was performed using a DM6000 microscope (Leica Microsystems Inc., IL, USA), and digital images were captured using a BFX365 camera.

Image Segmentation: To determine the dynamic change of RNV before and after treatment, image segmentation was performed to isolate the margin of the RNV. The algorithm for extracting the leakage area was reported by Schneider et al. 2012. This approach comprises three key steps. First, the original image (RGB scale) is converted into grayscale image. Afterward, multiple positions were chosen along the major blood vessels. Following this, the entire image is thresholded using these selected points as guides. Last, a vessel identifier algorithm is employed to isolate the vasculature bed from the image. Vessel density (VD) was determined by calculating all extracted pixels. Fluorescence intensity was measured from the isolated area using Image J and normalized with the pre-treatment.

Statistics Evaluation: Statistical analysis was performed using origin software (Origin 9, OriginLab Corporation, MA, USA). The data was expressed as mean ± SD. P value was determined using Anova. $P < 0.05$ is considered as significant difference between two independent groups.

Supporting Information

Supporting Information is available from the Wiley Online Library or from the author.

Acknowledgements

This work was funded by grants from the National Eye Institute (YMP: 1R01EY033000, 1R01EY034325, 1K08EY027458 & CHL: R01EY033000), Fight for Sight- International Retinal Research Foundation (YMP: FFSGIA16002), Alcon Research Institute Young Investigator Grant (YMP), unrestricted departmental support from Research to Prevent Blindness, and the Dr. Jonas Friedenwald Professorship in Ophthalmology (YMP). This research utilized the Core Center for Vision Research funded by the National Eye Institute (P30 EY001765). CHL also acknowledges the support from the Korea Institute for Advancement of Technology (KIAT) grant, funded by the Korea Government (MOTIE) (Global Industrial Technology Cooperation Center support program), for the development of transfer printing method and biodegradable devices. The authors would like to thank Drs. Yuqing Chen, Dongshan Yang, and the University of Michigan CAMTraST for the substantial donation of rabbits.

Conflict of Interest

YMP and CHL are co-inventors on a Purdue University and University of Michigan patent application on this technology. All of the other authors declare no competing financial interests.

Author Contributions

V.P.N., J.J., J.L., J.Z., C.H.L., and Y.M.P. conceived different aspects of the project, the concept of nanoneedles fabrication and interpreted experiments. V.P.N performed and analyzed data in vitro and in vivo experiments. J.J., J.L., J.Z., and C.H.L. contributed to fabricating and characterizing the soluble nanoneedles subconjunctival patch. V.P.N. and Z.M. conducted TUNNEL assay analysis. Z.W. performed immunofluorescence staining. J.Z., and M.Z. helped with OCT data analysis. The manuscript was written by V.P.N., J.Z., C.H.L., and Y.M.P. All authors have been involved in writing, reviewing, and revising of the manuscript.

Data Availability Statement

The data that support the findings of this study are available from the corresponding author upon reasonable request.

Keywords

anti-VEGF, biodegradable silicon nanoneedles, diabetic retinopathy (DR), optical coherence tomography (OCT), photoacoustic microscopy, retinal diseases, subconjunctival patch

Received: October 30, 2024
Revised: December 13, 2024
Published online:

[1] L. Guariguata, D. R. Whiting, I. Hambleton, J. Beagley, U. Linnenkamp, J. E. Shaw, *Diabetes Res. Clin. Pract.* **2014**, *103*, 137.
[2] Z. L. Teo, Y.-C. Tham, M. Yu, M. L. Chee, T. H. Rim, N. Cheung, M. M. Bikbov, Y. X. Wang, Y. Tang, Yi Lu, I. Y. Wong, D. S. W. Ting, G. S. W. Tan, J. B. Jonas, C. Sabanayagam, T. Y. Wong, C-Yu Cheng, *Ophthalmology* **2021**, *128*, 1580.
[3] T. Behl, A. Kotwani, *Pharmacol. Res.* **2015**, *99*, 137.
[4] P. F. Kador, M. Wyman, P. J. Oates, *Prog. Retinal Eye Res.* **2016**, *54*, 1.
[5] M. Kropp, O. Golubnitschaja, A. Mazurakova, L. Koklesova, N. Sargheini, T.-T. K. S. Vo, E. de Clerck, J. Polivka, P. Potuznik, J. Polivka, I. Stetkarova, P. Kubatka, G. Thumann, *EPMA J.* **2023**, *14*, 21.
[6] J. Cai, M. Boulton, *Eye* **2002**, *16*, 242.
[7] A. W. Stitt, T. M. Curtis, M. Chen, R. J. Medina, G. J. McKay, A. Jenkins, T. A. Gardiner, T. J. Lyons, H.-P. Hammes, R. Simó, N. Lois, *Prog. Retinal Eye Res.* **2016**, *51*, 156.
[8] E. J. Duh, J. K. Sun, A. W. Stitt, *JCI Insight* **2017**, *2*, e93751.
[9] A. Berger, T. Sheidow, A. F. Cruess, J. D. Arbour, A.-S. Courseau, F. de Takacsy, *Can. J. Ophthalmol.* **2015**, *50*, 209.
[10] P. Mitchell, F. Bandello, U. Schmidt-Erfurth, G. E. Lang, P. Massin, R. O. Schlingemann, F. Sutter, C. Simader, G. Burian, O. Gerstner, A. Weichselberger, *Ophthalmology* **2011**, *118*, 615.
[11] M. J. Elman, L. P. Aiello, R. W. Beck, N. M. Bressler, S. B. Bressler, A. R. Edwards, F. L. Ferris, S. M. Friedman, A. R. Glassman, K. M. Miller, I. U. Scott, C. R. Stockdale, J. K. Sun, *Ophthalmology* **2010**, *117*, 1064.
[12] N. Ferrara, L. Damico, N. Shams, H. Lowman, R. Kim, *Retina* **2006**, *26*, 859.
[13] S. J. Bakri, M. R. Snyder, J. M. Reid, J. S. Pulido, M. K. Ezzat, R. J. Singh, *Ophthalmology* **2007**, *114*, 2179.
[14] S. J. Bakri, M. R. Snyder, J. M. Reid, J. S. Pulido, R. J. Singh, *Ophthalmology* **2007**, *114*, 855.
[15] J. Gaudreault, D. Fei, J. C. Beyer, A. Ryan, L. Rangell, V. Shiu, L. A. Damico, *Retina* **2007**, *27*, 1260.
[16] C. Sramek, M. Mackanos, R. Spitler, L.-S. Leung, H. Nomoto, C. H. Contag, D. Palanker, *Invest. Ophthalmol. Visual Sci.* **2011**, *52*, 1780.
[17] K. Rohrschneider, S. Bültmann, R. Glück, F. E. Kruse, T. Fendrich, H. E. Völcker, *Am. J. Ophthalmol.* **2000**, *129*, 27.
[18] T. Moutray, J. R. Evans, N. Lois, D. J. Armstrong, T. Peto, A. Azuara-Blanco, *Cochrane Database of Systematic Reviews* **2018**.
[19] J. Candiello, G. J. Cole, W. Halfter, *Matrix Biol.* **2010**, *29*, 402.
[20] K. Peynshaert, H. Vanluchene, K. De Clerck, An-K Minnaert, M. Verhoeven, N. Gouspillou, N. Bostan, T. Hisatomi, G. Accou, F.

Sauvage, K. Braeckmans, S. De Smedt, K. Remaut, *J. Controlled Release* **2022**, *349*, 315.
[21] K. Takahashi, T. Igarashi, K. Miyake, M. Kobayashi, C. Yaguchi, O. Iijima, Y. Yamazaki, Y. Katakai, N. Miyake, S. Kameya, T. Shimada, H. Takahashi, T. Okada, *Mol. Ther.* **2017**, *25*, 296.
[22] W. Park, V. P. Nguyen, Y. Jeon, B. Kim, Y. Li, J. Yi, H. Kim, J. W. Leem, Y. L. Kim, D. R. Kim, Y. M. Paulus, C. H. Lee, *Sci. Adv.* **2022**, *8*, eabn1772.
[23] C. Chiappini, Y. Chen, S. Aslanoglou, A. Mariano, V. Mollo, H. Mu, E. De Rosa, G. He, E. Tasciotti, Xi Xie, F. Santoro, W. Zhao, N. H. Voelcker, R. Elnathan, *Nat. Protoc.* **2021**, *16*, 4539.
[24] S. Gopal, C. Chiappini, J. Penders, V. Leonardo, H. Seong, S. Rothery, Y. Korchev, A. Shevchuk, M. M. Stevens, *Adv. Mater.* **2019**, *31*, 1806788.
[25] H. Kim, H. Jang, B. Kim, M. K. Kim, D. S. Wie, H. S. Lee, D. R. Kim, C. H. Lee, *Sci. Adv.* **2018**, *4*, eaau6972.
[26] S.-W. Hwang, Hu Tao, D.-H. Kim, H. Cheng, J.-K. Song, E. Rill, M. A. Brenckle, B. Panilaitis, S. M. Won, Y.-S. Kim, Y. M. Song, K. J. Yu, A. Ameen, R. Li, Y. Su, M. Yang, D. L. Kaplan, M. R. Zakin, M. J. Slepian, Y. Huang, F. G. Omenetto, J. A. Rogers, *Science* **2012**, *337*, 1640.
[27] L. Yin, A. B. Farimani, K. Min, N. Vishal, J. Lam, Y. K. Lee, N. R. Aluru, J. A. Rogers, *Adv. Mater.* **2015**, *27*, 1857.
[28] S.-K. Kang, R. K. J. Murphy, S.-W. Hwang, S. M. Lee, D. V. Harburg, N. A. Krueger, J. Shin, P. Gamble, H. Cheng, S. Yu, Z. Liu, J. G. McCall, M. Stephen, H. Ying, J. Kim, G. Park, R. C Webb, C. H. Lee, S. Chung, D. S. Wie, A. D. Gujar, B. Vemulapalli, A. H. Kim, K.-M. Lee, J. Cheng, Y. Huang, S. H. Lee, P. V. Braun, W. Z. Ray, J. A. Rogers, *Nature* **2016**, *530*, 71.
[29] S. Prahl, **2024**, *2024*.
[30] V. P. Nguyen, Y. M. Paulus, *J. Imaging* **2018**, *4*, 149.
[31] K. Ghasemi Falavarjani, Q. Nguyen, *Eye* **2013**, *27*, 787.
[32] R. D. Jager, L. P. Aiello, S. C. Patel, E. T. Cunningham Jr, *Retina* **2004**, *24*, 676.
[33] M. Amer, R. K. Chen, *Macromol. Biosci.* **2020**, *20*, 2000089.
[34] J. Jiang, H. S. Gill, D. Ghate, B. E. McCarey, S. R. Patel, H. F. Edelhauser, M. R. Prausnitz, *Invest. Ophthalmol. Visual Sci.* **2007**, *48*, 4038.
[35] P. Gupta, K. S. Yadav, *Life Sci.* **2019**, *237*, 116907.
[36] K. Kadonosono, S. Yamane, A. Arakawa, M. Inoue, T. Yamakawa, E. Uchio, Y. Yanagi, S. Amano, *JAMA ophthalmol.* **2013**, *131*, 783.
[37] V. P. Nguyen, W. Qian, Y. Li, B. Liu, M. Aaberg, J Henry, W. Zhang, X. Wang, Y. M. Paulus, *Nat. Commun.* **2021**, *12*, 34.
[38] V. P. Nguyen, W. Qian, J. Zhe, j. Henry, M. Wang, B. Liu, W. Zhang, X. Wang, Y. M. Paulus, *Adv. Mater.* **2023**, *35*, 2302069.
[39] V. P. Nguyen, A. J. Karoukis, W. Qian, L. Chen, N. D. Perera, D. Yang, Q. Zhang, J. Zhe, J. Henry, B. Liu, W. Zhang, A. T. Fahim, X. Wang, Y. M. Paulus, *ACS Nano* **2024**, *18*, 14893.
[40] V. P. Nguyen, J. Henry, J. Zhe, J. Hu, X. Wang, Y. M. Paulus, *Sci. Rep.* **2023**, *13*, 8396.
[41] V. P. Nguyen, A. J. Karoukis, J. Hu, Z. Wei, D. Yang, A. T. Fahim, X. Wang, Y. M. Paulus, *Sci. Rep.* **2024**, *14*, 19457.
[42] V. P. Nguyen, J. Hu, J. Zhe, E. Y. Chen, D. Yang, Y. M. Paulus, *Sci. Rep.* **2023**, *13*, 22071.
[43] V. P. Nguyen, W. Fan, T. Zhu, W. Qian, Y. Li, B. Liu, W. Zhang, J. Henry, S. Yuan, X. Wang, Y. M. Paulus, *ACS Nano* **2021**, *15*, 13289.
[44] V.-P. Nguyen, et al., *ACS Appl. Mater. Interfaces* **2021**, *13*, 40214.
[45] Y. Yu, Yu Qin, J. Fu, Y. Li, W. Zhang, T. Zhu, L. Jiang, X. Wang, Y. M. Paulus, *Exp. Eye Res.* **2021**, *207*, 108577.
[46] Z. Xie, X. Wu, R. Cheng, J. Huang, X. Wang, Q. Shi, B. Xu, Y. M. Paulus, S. Yuan, Q. Liu, *Exp. Eye Res.* **2023**, *228*, 109388.
[47] S. C. Keating, A. A. Thomas, P. A. Flecknell, M. C. Leach, *PLoS One* **2012**, *7*, e44437.